Energy Compression of Dielectric Barrier Discharge With Third Harmonic Circulating Current in Current-Fed Parallel-Series Resonant Converter

Shiqiang Hao, Xingliang Liu, Wuhua Li, Yan Deng, and Xiangning He, *Fellow, IEEE*

***Abstract*—An advanced technique of energy compression with the third harmonic circulating current generation is presented in this paper to improve the surface treatment performance in the dielectric barrier discharge (DBD) systems. First, the relationship between the energy compression degree and contact angle is explored, which shows that the polymer surface wettability can be improved by the high energy compression degree in DBD. And then, an additional inductor is inserted into the resonant tank in the current-fed parallel-series resonant converter to generate the third harmonic current component, which can reduce the discharge-time-ratio and compress the energy transferred to the DBD loads. Furthermore, the method of rectifier-compensated fundamental plus third harmonic approximation (RCFTHA) is introduced to describe the current-fed parallel-series resonant converter by superposing two equivalent linear circuits operating at the fundamental and third harmonic frequencies, respectively. Consequently, the discharge-time-ratio optimization with the parallel-series resonant tank design is realized. Finally, the experimental results from a 350-W prototype substantiate the effectiveness of the energy compression with the third harmonic circulating current and the accuracy of RCFTHA.**

***Index Terms*—Current-fed parallel-series resonant converter, dielectric barrier discharge, discharge-time-ratio, energy compression, third harmonic circulating current.**

NOMENCLATURE

C_d, C_g	Equivalent dielectric barrier and air gap capacitors.
V_T	Discharge maintaining voltage of DBD.
p_o	Instantaneous real power transferred to the DBD load.
$P_{o-\mathrm{av}}$	Average real power transferred to the DBD load.
n	Transformer turns ratio, $N_{\mathrm{sec}}/N_{\mathrm{pri}}$.
v_{Cg}	Voltage across the air gap.
v_o, i_o	Voltage and current of the DBD load.
v_{AB}	H-inverter output voltage in the current-fed resonant converter.
i_{o1}, i_{o3}	Fundamental and third harmonic components of the load current i_o.
$i_{\mathrm{exc}}, i_{\mathrm{excs}}$	Excitation square-wave currents of the parallel-series resonant tank referred to the primary and the secondary sides respectively, $i_{\mathrm{exc}} = n i_{\mathrm{excs}}$.
i_{exc1}	Fundamental component of the square-wave current i_{exc}.
i_{o-v}	Virtual piecewise rectangular current for wave shape estimation.
Δt_{ps}	Time interval between the zero crossing points of voltage v_{AB} and current i_{exc}.
Δt_{dis}	Active discharge time in a half period $1/2T_s$.
$\Delta t_{\mathrm{dis-sin}}$	Active discharge time in a half period $1/2T_s$ in the sinusoidal CCM.
Δt_{zs}	Time interval between the zero crossing points of i_o and v_o.
$\Delta t_{\mathrm{dis}-v}$	Virtual discharge time of the rectangular current i_{o-v}.
k_{dis}	Discharge-time-ratio, ratio of Δt_{dis} to $1/2T_s$, $k_{\mathrm{dis}} = 2\Delta t_{\mathrm{dis}}/T_s$.
$k_{\mathrm{dis-sin}}$	Discharge-time-ratio in the sinusoidal CCM, $k_{\mathrm{dis-sin}} = 2\Delta t_{\mathrm{dis-sin}}/T_s$.
k_{zs}	Zero-crossing-shift coefficient, ratio of Δt_{zs} to $1/2T_s, k_{\mathrm{zs}} = 2\Delta t_{\mathrm{zs}}/T_s$.
k_v	Virtual discharge-time-ratio of $i_{\mathrm{o-v}}$, ratio of $\Delta t_{\mathrm{dis}-v}$ to $1/2T_s, k_v = 2\Delta t_{\mathrm{dis}-v}/T_s$.
λ	Energy compression degree, ratio of $k_{\mathrm{dis-sin}}$ to k_{dis}, $\lambda = k_{\mathrm{dis-sin}}/k_{\mathrm{dis}}$.
C_p, C_{ps}	Parallel resonant capacitors of the parallel-series resonant tank referred to the primary and the secondary sides respectively, $C_{\mathrm{ps}} = C_p/n^2$.
L_s, L_{ss}	Series resonant inductor of the resonant tank referred to the primary and the secondary sides respectively, $L_{\mathrm{ss}} = L_s n^2$.
L_m, L_{ms}	Transformer magnetizing inductors of the parallel-series resonant tank referred to the primary and the secondary sides respectively, $L_{\mathrm{ms}} = L_m n^2$.
T_s, f_s	Switching period and frequency of the inverter for DBD, $f_s = 1/T_s$.

Manuscript received June 01, 2015; revised August 28, 2015 and December 02, 2015; accepted January 12, 2016. Date of publication January 22, 2016; date of current version July 08, 2016. This work was supported by the National Nature Science Foundation of China (51277195). Recommended for publication by Associate Editor F. Costa.

The authors are with the College of Electrical Engineering, Zhejiang University, Hangzhou 310027, China (e-mail: sqhowe98@163.com; lxlwxkj@gmail.com; woohualee@zju.edu.cn; Dengyan@zju.edu.cn; hxn@zju.edu.cn).

Color versions of one or more of the figures in this paper are available online at http://ieeexplore.ieee.org.

Digital Object Identifier 10.1109/TPEL.2016.2520953

I. INTRODUCTION

THE dielectric barrier discharge (DBD) is a type of high voltage discharge occurring between two electrodes with an inserted insulating dielectric barrier [1]–[4], which is extensively used in the surface treatment of the polymer, glass, textiles, and other materials [5]–[9]. The surface treatment equipment in the atmospheric-pressure air is shown in Fig. 1(a). The grounded roller is covered with a rubber casing as the

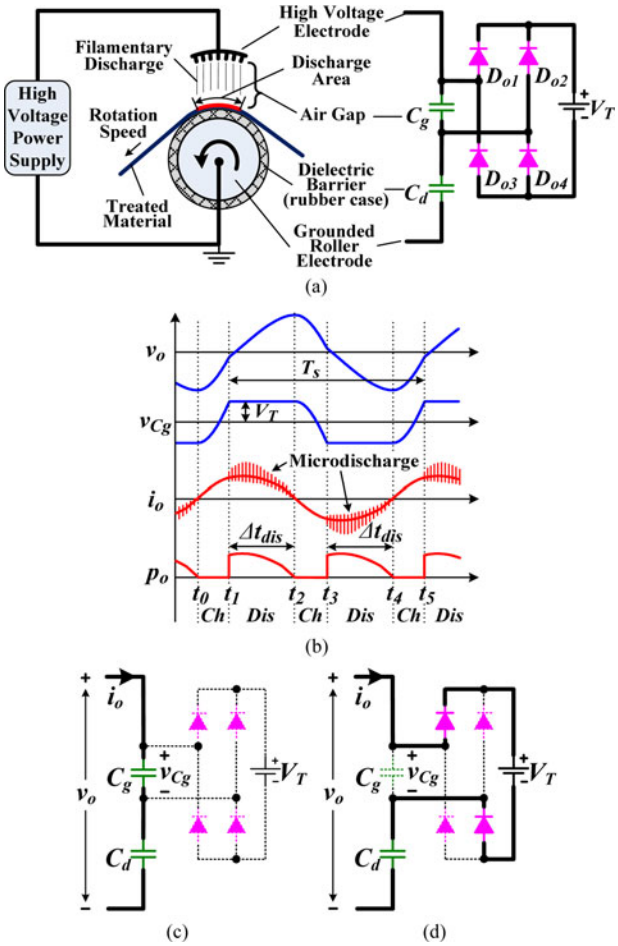

Fig. 1. DBD surface treatment equipment's model and operation principle: (a) left view of the equipment structure and its equivalent circuit; (b) waveforms of v_o, i_o, v_{Cg} and p_o; (c) charge stage; and (d) discharge stage.

dielectric barrier and rotates together with the film material. An alternating-current (ac) voltage up to 20 kV at 10–50 kHz is applied to the knife-edge electrode [10]. When the voltage is high enough, the air gap between the high voltage electrode and the dielectric breaks down, producing a filamentary discharge. Then, the low temperature plasma is generated in the gap to react with the material and cause the physical and chemical changes on the material surface, such as the roughening, etching, and oxidation. After passing through the gap, the treated material becomes receptive to printing inks, coatings, and adhesives. The electrode configuration is often modeled by the circuit in Fig. 1(a), where C_g and C_d represent the equivalent capacitances of the air gap and the dielectric barrier, respectively [2]–[5]. Fig. 1(b) shows the waveforms of the ac output voltage v_o, output current i_o, gap voltage v_{Cg}, and instantaneous real power p_o. Unlike v_o and i_o, the gap voltage v_{Cg} cannot be directly measured using a voltage probe but can be derived from v_o with the defined C_d and C_g. When the gap voltage v_{Cg} is smaller than the discharge maintaining voltage V_T, C_g is charged with the turned-off equivalent rectifier diodes D_{o1}–D_{o4} as in Fig. 1(c). During this charge stage, there is no discharge in the gap and no real power flowing through the circuit. When v_{Cg} reaches V_T, v_{Cg} is clamped to V_T as in Fig. 1(d) and the discharge occurs until i_o reduces to zero. During this discharge stage $\Delta t_{\rm dis}$, the numerous pulsed microdischarge currents appear in i_o as in Fig. 1(b) and the real power is consumed by the gap.

For a fixed electrode structure in the atmospheric-pressure air, the treatment effect is mainly affected by two factors. One is the power density, which is calculated by dividing the average output power by the discharge area on the dielectric surface in Fig. 1(a) [11]. The other is the treatment time taken by the sample to pass through the gap and be exposed to the discharge [12]–[14], which is controlled by the roller rotation speed. For convenience, the two variables are combined as a concept of "plasma dose density," which is the product of power density and treatment time [7], [8]. The impact of the dose density has been substantially analyzed. It is concluded that the treatment effect can be improved by increasing the dose density until reaching the saturation state [12]. The active time of transferring the dose to the gap is the discharge time $\Delta t_{\rm dis}$, which is available per repetitive cycle as shown in Fig. 1(b) and different from the "treatment time." Unfortunately, the influence of the discharge time $\Delta t_{\rm dis}$ is rarely discussed. This paper investigates the relationship between the treatment effect and dose transfer time by using a concept of discharge-time-ratio, which refers to the ratio of the discharge time to the period. In this paper, the reduction of discharge-time-ratio under the constant average power is proved to promote the treatment effect, which brings economic benefits and practical values.

As the DBD load, the electrode configuration in Fig. 1 cannot determine the discharge-time-ratio by itself, which depends on the high voltage power supply. Compared with the pulse generators in [16]–[18], the resonant converter with a high step-up ratio transformer [3], [6], [15] has lower current stress on power devices, better electromagnetic interference performance and more flexible control, making it an effective and reliable solution. Most commercial resonant power supplies operate in a continuous current mode (CCM) and produce an approximately sinusoidal current through the DBD load as in Fig. 1(b) [5], [6], which is called the sinusoidal CCM. The discharge-time-ratio in this case is fixed at the certain frequency and power. Under the condition that both the average output power and operating frequency remain unchanged, reducing or increasing the discharge-time-ratio in the sinusoidal CCM through different solutions can be viewed as the energy compression or stretching, respectively. To make the discharge-time-ratio adjustable, the resonant converter needs to output a nonsinusoidal waveform. There are two ways to implement this function: the discontinuous current mode (DCM) and the higher harmonic injection into the DBD load. If the resonant inductance is sufficiently small, the discharge-time-ratio can be theoretically reduced to close to zero in the DCM [3]. This study uses the DCM to explore the interaction between the treatment effect and discharge-time-ratio, and concludes that the treatment effect can be enhanced by the energy compression. However, the DCM is associated with higher current stress on the power devices than with the CCM, which limits its high power application. If a higher harmonic current is injected into the load to reshape the original sinusoidal waveform, the discharge-time-ratio can also become adjustable

while the current stress is similar to that with the sinusoidal CCM.

Since connecting the power supply with another independent harmonic source is difficult to realize, the single resonant converter is employed to generate a harmonic. The voltage-fed resonant topology has a simple inverter structure and flexible control schemes [3], [5], [19], [20], but its short-circuit survival ability is weaker than that of a current-fed topology [15], [21], [22], which is crucial to the power supply life time and the normal treatment process [22]. The current-fed parallel resonant topology in [22] outputs an approximately sinusoidal waveform and eliminates most harmonics. By adding an inductor in series with the transformer leakage inductor, the parallel resonant tank in [22] is turned into a parallel-series structure that generates a third harmonic circulating current. The resonant parameters should be assigned based on the discharge-time-ratio. The piecewise mathematical approach in [3], [22], and [23] gives accurate design results, but requires considerable calculation. The fundamental harmonic approximation (FHA) [24] and the rectifier-compensated FHA (RCFHA) [25], [26] require less calculation but do not describe the third harmonic component. A rectifier-compensated fundamental plus third harmonic approximation (RCFTHA) method is introduced to describe the current-fed parallel-series resonant converter by superposing two equivalent linear subcircuits operating at the fundamental and third harmonic frequencies, respectively.

This study develops an energy compression technique for DBD performance improvement with the third harmonic circulating current, which is established in a current-fed parallel-series resonant converter and designed on the base of a linear circuit superposition method (RCFTHA). The relationship between the contact angle and energy compression degree is explored in Section II. The third harmonic circulating current principle is introduced in Section III. The parameter design based on the RCFTHA for the energy compression is summarized in Section IV. The experimental verification is shown in Section V. The final section summarizes the investigation.

II. Relationship Between Contact Angle and Energy Compression Degree in DBD Systems

The contact angle is a quantitative measure of the material surface wettability, which is a specialized term in material science and measured using the liquid droplet on the material surface [8]. Smaller contact angle indicates better surface treatment effect. The discharge-time-ratio $k_{\rm dis}$ is the ratio of discharge time $\Delta t_{\rm dis}$ to half period $1/2T_s$. At the given power and frequency, the energy in each period $T_{\rm s}$ is a constant value and the reduction of $\Delta t_{\rm dis}$ or $k_{\rm dis}$ is called the energy compression. The energy compression degree λ is defined by using the discharge-time-ratio $k_{\rm dis-sin}$ in the sinusoidal CCM ($i_{\rm o}$ is sinusoidal as in Fig. 1) as the reference, which is expressed as the ratio of the $k_{\rm dis-sin}$ to a $k_{\rm dis}$ with any load current shape. It should be noted that $k_{\rm dis}$ and $k_{\rm dis-sin}$ are compared under the condition that the period T_s and average power $P_{o-{\rm av}}$ are the same in the two cases. If λ is larger than 1, the energy is compressed. Otherwise, the energy is stretched.

The relationship between the contact angle and the energy compression degree is assessed by using the voltage-fed series resonant circuit in DCM [3], as shown in Fig. 2(a). The ac utility power is rectified, filtered, and then, converted by a front-end buck circuit to provide a direct-current (dc) voltage $V_{\rm dc}$ for the H-bridge inverter. The power is regulated by using the buck circuit with the pulse width modulation (PWM). The inverter operates at a constant switching frequency of 30 kHz. An additional variable inductor L_{s1} is connected in series with the transformer leakage inductor L_{s2} to adjust $k_{\rm dis}$ over a wide range. L_{s1} and L_{s2} compose the total series inductor L_s. Fig. 2(b) presents the typical waveforms of transformer output voltage v_o and current i_o. During the discharge, the microdischarge currents appear in i_o, which is shown with a fivefold expansion in Fig. 2(b). The waveforms of the primary inverter output voltage $v_{\rm pri}$ and current $i_{\rm pri}$ are in Fig. 2(c). $\Delta t_{\rm dis}$ depends on L_s and decreases with decreased L_s [3].

The treatment time (s) is set as 0.6 s. The active discharge area (cm^2) of the DBD load is 176 cm^2. Thus, the dose density (J/cm^2) is controlled by the average output real power (W) $P_{o-{\rm av}}$ [8]. Three $P_{o-{\rm av}}$ values of 250, 300, and 350 W are selected for assessing the energy compression effect, which can deduce three dose densities of 0.852, 1.023, and 1.193 J/cm^2, respectively. The enveloped area of the voltage/charge Lissajous figure is measured from the DBD load in Fig. 2(a) to calculate the value of $P_{o-{\rm av}}$ [5], [8], [10]. Moreover, $k_{\rm dis}$ can be adjusted by changing L_{s1}. The polyethylene (PE) film material was treated at the three dose densities and different discharge-time-ratios. Nine test points were selected on one material sample to measure nine water contact angles, which were then averaged to one final value. The average measured contact angles at different dose densities and $k_{\rm dis}$ values are illustrated in Fig. 2(d). The largest $k_{\rm dis}(k_{\rm dis-sin})$ at each dose density was achieved when operating in the sinusoidal CCM. The contact angles in the sinusoidal CCM are marked in Fig. 2(d) to be the comparison objects. At the same dose density, smaller contact angle and better surface wettability are attained with smaller $k_{\rm dis}$. The lowest contact angle is achieved at the highest λ of 4.82. Thus, the energy compression improves the treatment effect of the sinusoidal CCM.

Fig. 2(e) presents the peak values of the primary inverter output current $i_{\rm pri}$ measured at different $k_{\rm dis}$ to indicate the increase of the power device current stress brought by the energy compression with DCM. The DCM resonant converter has higher current stress than the CCM converter and the current stress increases sharply with decreased $k_{\rm dis}$, which impacts the power device selection and limits its high power application. The reason for the high current stress is the high reactive power returned from the resonant tank to the input dc source in DCM as shown in Fig. 2(c).

III. Energy Compression With Third Harmonic Circulating Current

Another approach should be explored to achieve an energy compression effect similar to the DCM but endure lower current stress. As illustrated in Section II, reshaping the load current

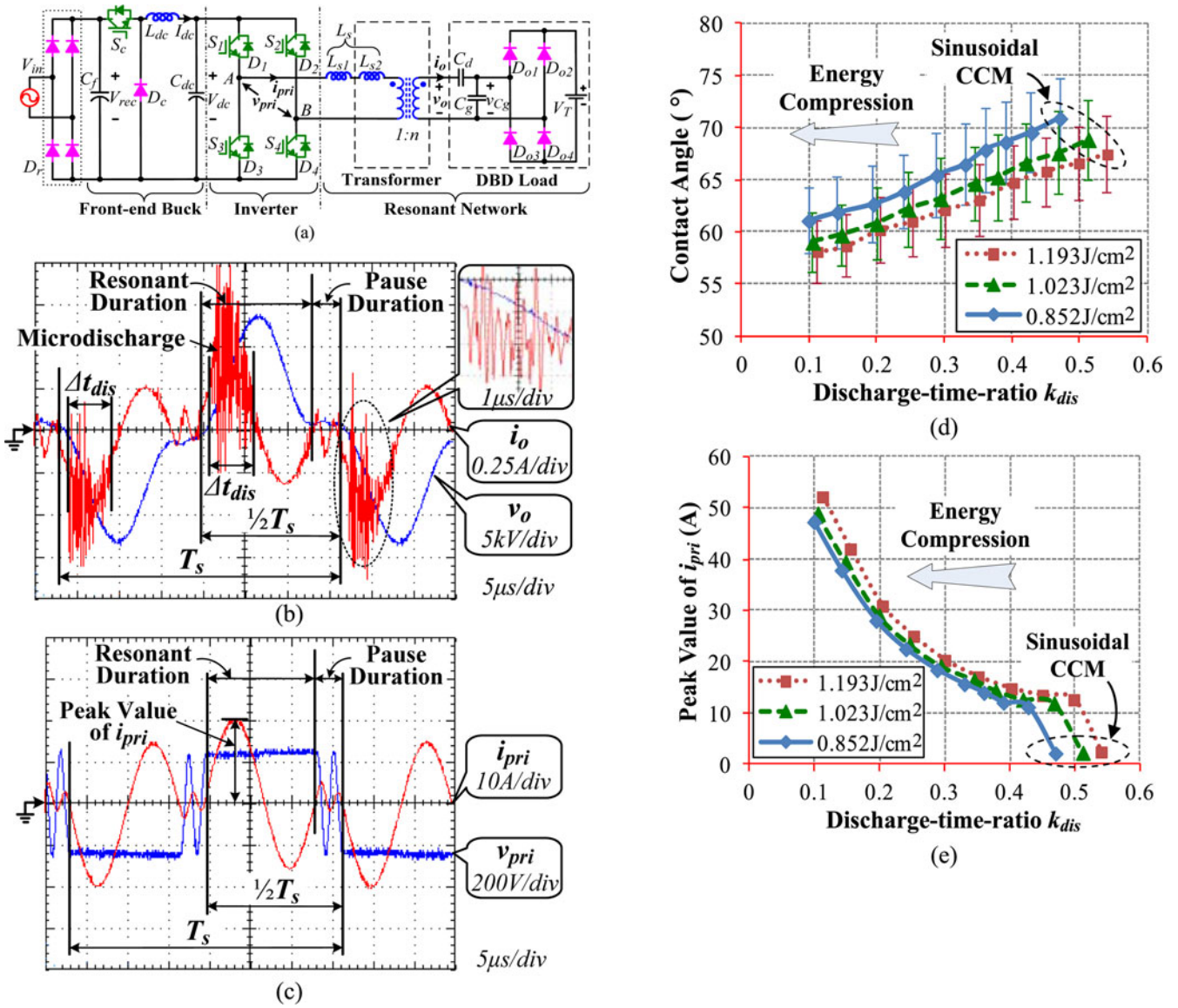

Fig. 2. Assessing of energy compression effect: (a) voltage-fed series resonant converter; (b) v_o and i_o in DCM; (c) $v_{\rm pri}$ and $i_{\rm pri}$ in DCM; (d) correlation among contact angle, discharge-time-ratio and plasma dose density; and (e) peak currents of $i_{\rm pri}$ at different dose densities and discharge-time-ratios.

into a nonsinusoidal waveform can reduce the discharge-time-ratio. Fig. 3 presents two cases for comparison: the typical DCM waveforms with solid lines and the waveforms consisting of two harmonic components with dashed lines. The typical load current i_o in DCM is shaped like the superposition of a fundamental component i_{o1} and a third harmonic component i_{o3} in Fig. 3. It would not affect the subsequent analysis by omitting the mircodischarge currents. If the superposed current $(i_{o1}+i_{o3})$ is injected into the load in Fig. 1, it can yield a gap voltage v_{Cg} similar to that in the DCM as shown in Fig. 3. Moreover, provided the current amplitudes of i_{o1} and i_{o3} are set appropriately, the discharge time $\Delta t_{\rm dis}$ value and the instantaneous power p_o waveform generated by this superposed current can be the same as those in the DCM as shown in Fig. 3. The waveform of p_o in the sinusoidal CCM is also drawn in Fig. 3 as a reference. Both the harmonic superposition and DCM can decrease the dose transfer time in $1/2T_s$ from $\Delta t_{\rm dis-sin}$ to a smaller $\Delta t_{\rm dis}$. Hence, injecting a third harmonic current into a sinusoidal CCM DBD system can also realize the energy compression.

Operating in the resonant state, the current-fed converter with a parallel resonant tank in [22] eliminates higher harmonics, which is similar to the circuit structure in Fig. 5(a) but has no series inductor L_s. By inserting this inductor L_s into the resonant tank as in Fig. 5(a), the current-fed parallel resonant converter in [22] is turned into a current-fed parallel-series resonant converter that generates a third harmonic circulating current. Before detailing this parallel-series resonant converter, the third harmonic current generation needs to be first explained by using a simplified circuit form in Fig. 4(a), where the resonant tank is regarded as the combination of a compensation network and the load capacitances. All parameters in Fig. 4 are referred to the transformer secondary side. With the series resonant

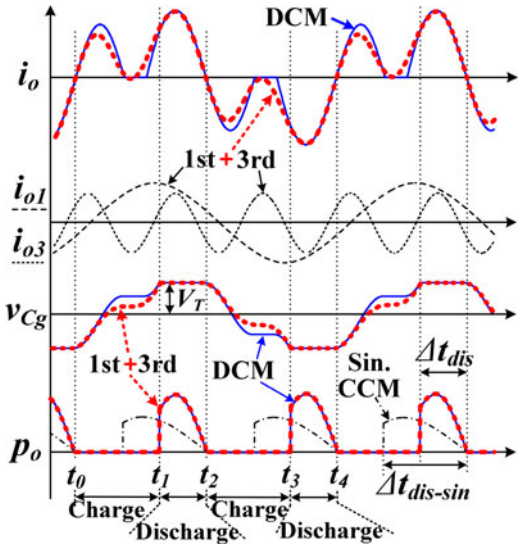

Fig. 3. Approximation of DCM by the superposition of fundamental current and third harmonic current.

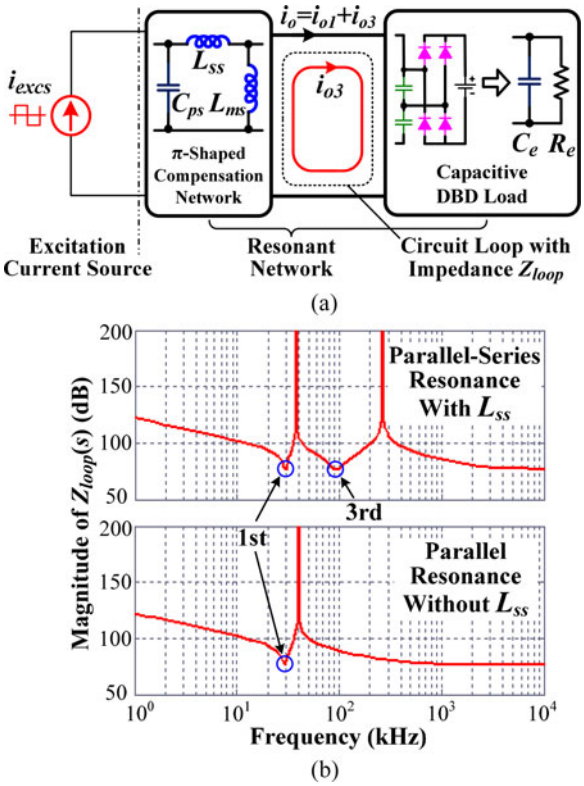

Fig. 4. Third harmonic circulating current generation principle in parallel-series resonant tank: (a) simplified circuit form containing a circuit loop and (b) magnitude-frequency characteristics of $Z_{\rm loop}$ with and without $L_{\rm ss}$.

inductor $L_{\rm ss}$, the circuit in Fig. 4(a) is the simplified form of the current-fed parallel-series resonant converter, which has a π-shaped compensation network. But with no $L_{\rm ss}$, the circuit in Fig. 4(a) becomes the simplified form of the parallel resonant converter in [22]. Then, the third harmonic current generation is explained as follows.

First, the source of the third harmonic current is the DBD nonlinear behavior. In the actual circuit, the DBD load has an

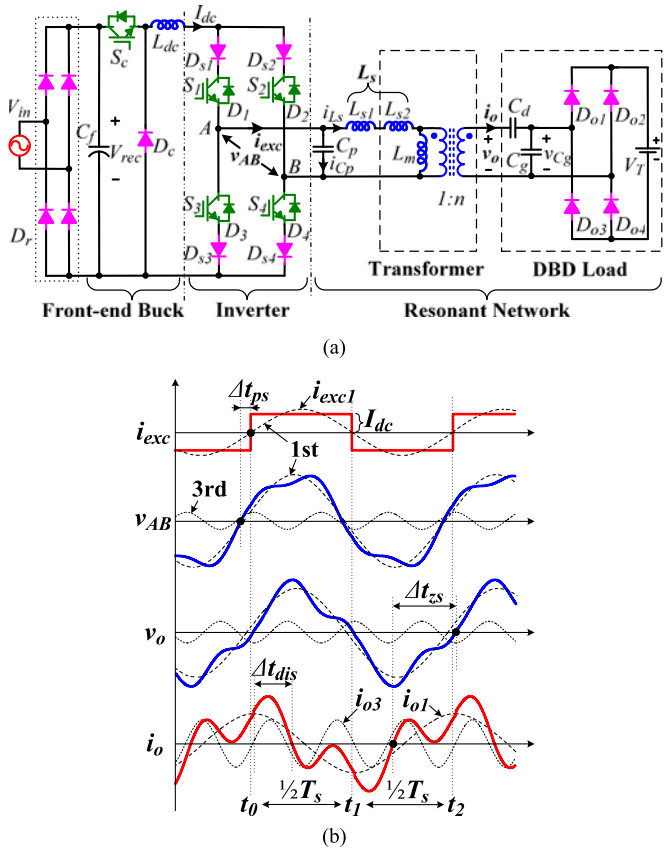

Fig. 5. Current-fed parallel-series resonant converter: (a) circuit configuration and (b) time domain waveforms.

equivalent diode rectifying behavior as in Fig. 1, making it a nonlinear rectifier load. The current through the DBD load has a tendency to produce the distortion and higher harmonic components.

Second, a flow path (not source) for the third harmonic current exists in the resonant tank, which cannot be analyzed by using the DBD nonlinearity in the accurate model. To discuss the current flow paths, the resonant tank should be analyzed at various frequencies, especially at the third harmonic frequency, which is difficult for a circuit with the nonlinear DBD model in Fig. 1. Only if the DBD load is modeled by a linear equivalent circuit, the classical frequency-domain approaches like the transfer function and Bode diagram can be employed here to qualitatively analyze the resonant tank characteristics at various frequencies [27]. Since the DBD load is considered capacitive, it can be approximated by a parallel combination of capacitor C_e and resistor R_e as in [1]. The compensation network and the load compose a circuit loop as shown with a dashed loop line in Fig. 4(a). A loop circuit impedance $Z_{\rm loop}$ is defined as the sum of the compensation network impedance and load impedance. $Z_{\rm loop}$ represents the filtering effect of the circuit loop on each frequency component of the load current. The $R_e//C_e$ linear model is used to plot the Bode diagram of $Z_{\rm loop}$. Fig. 4(b) compares the theoretical magnitude-frequency characteristics of $Z_{\rm loop}$ with and without $L_{\rm ss}$. The phase of $Z_{\rm loop}$ is omitted for its uselessness to the discussion on the circuit loop filtering

effect. For the parallel resonant tank without $L_{\rm ss}$, the magnitude-frequency characteristic of $Z_{\rm loop}$ has only one valley point at the resonant frequency as shown in Fig. 4(b). For the parallel-series resonant tank with $L_{\rm ss}$, the magnitude-frequency characteristic of $Z_{\rm loop}$ has two valley points at two different frequencies in Fig. 4(b), which shows that the insertion of $L_{\rm ss}$ causes two resonances in this resonant tank. By selecting appropriate resonant parameters, the lower and higher resonant frequencies can be designed as the fundamental and third harmonic frequencies, respectively. Thus, the parallel-series resonant tank can provide a low-impedance circular path for the third harmonic current but the parallel resonant tank filters it to a negligible degree.

To sum up, a third harmonic current i_{o3} produced by the DBD nonlinearity is proved to be absorbed into the low-impedance circular path in the parallel-series resonant tank. i_{o3} only circulates along the circuit loop inside the resonant tank as shown in Fig. 4(a) and does not flow through the excitation source.

The simplified circuit form in Fig. 4(a) can be instantiated as the current-fed parallel-series resonant converter in Fig. 5(a). The ac grid power is rectified, filtered, and then, converted by a front-end buck circuit to provide a dc current $I_{\rm dc}$. The power is regulated through the buck circuit with the PWM that controls the amplitude of $I_{\rm dc}$. The current-fed H-bridge circuit inverts $I_{\rm dc}$ to an ac current $i_{\rm exc}$ to excite the resonant tank. By detecting the zero crossing point of the H-inverter output voltage $v_{\rm AB}$, a phase-locked loop controller automatically adjusts the H-bridge operating frequency to maintain a small fixed time interval $\Delta t_{\rm ps}$ between the zero crossing points of $v_{\rm AB}$ and $i_{\rm exc}$ [2]. This phase-locked loop technique makes $v_{\rm AB}$ and $i_{\rm exc}$ almost in phase, lowering the switching losses [22]. A step-up transformer with a turns ratio n is used. The resonant tank is derived from the parallel resonant configuration in [22] by integrating the transformer leakage inductor L_{s2} and an additional inductor L_{s1} into the resonant tank. L_{s1} and L_{s2} compose the series inductor L_s. The parallel-series resonant network comprises the parallel capacitor C_p, series inductor L_s, transformer magnetizing inductor L_m, and DBD load equivalent capacitors. Fig. 5(b) shows the typical waveforms. The dc inductance $L_{\rm dc}$ is sufficiently large, allowing $i_{\rm exc}$ to be treated as a square-wave current. A small time interval $\Delta t_{\rm ps}$ exists between the zero crossing points of $v_{\rm AB}$ and $i_{\rm exc}$ due to the phase-locked loop control. Through the harmonic analysis, the waveforms of $v_{\rm AB}$, v_o, and i_o are mainly formed by the superposition of the fundamental and third harmonic components as in Fig. 5(b), and other frequency components are negligible. Another time interval $\Delta t_{\rm zs}$ represents the time by which the zero crossing point of i_o leads that of v_o. A coefficient $k_{\rm zs}$ is defined as the ratio of $\Delta t_{\rm zs}$ to half period $1/2T_s$, which is called the zero-crossing-shift coefficient and is important for the parameter design in Section IV.

The third harmonic current circulation is actually a solution to adjust the current wave shape. The control of the resonant converter in Fig. 5(a) has two functions: the power regulation with PWM in the buck circuit and the phase-lock control in the H-inverter. The third harmonic current, circulating only inside the resonant tank, is not related to the controls of the buck circuit and the H-inverter. Both the amplitude and the phase of the third harmonic circulating current at the given power and frequency depend on the resonant tank parameters: C_p, L_s and L_m to be designed in Section IV. So the third harmonic current circulation is an issue in terms of circuit design rather than active control.

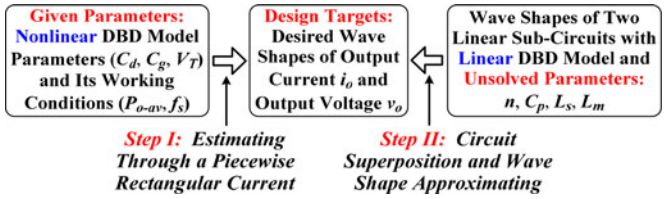

Fig. 6. Flowchart of RCFTHA.

The converter in Fig. 5 operates in the CCM with the phase-locked control, reducing the reactive power returned from the resonant tank. The third harmonic load current only circulates inside the resonant tank and the H-inverter carries a square-wave current, reducing the current peak through the switches. So the energy compression with third harmonic circulating current does not increase the inverter current stress.

IV. Design Consideration for Energy Compression

The nonlinear DBD model parameters (C_d, C_g, V_T) and its working conditions $(P_{o\text{–av}}, f_s)$ should be given according to the specifications before the design. And four key parameters, including n, C_p, L_s, and L_m, should be designed. Fig. 6 illustrates the proposed RCFTHA design process, which is divided into two steps. In the first step, the desired wave shapes of output current i_o and output voltage v_o are estimated by using a virtual piecewise rectangular load current $i_{o\text{–}v}$. These estimated current and voltage wave shapes serve as the design targets of the next step. In the second step, two linear equivalent sub-circuits operating at f_s and $3f_s$ are first established by using a linear DBD model. Then, the waveforms of the two sub-circuits are superposed to realize the desired wave shapes of i_o and v_o estimated from the current $i_{o\text{–}v}$ in the first step, which is called the wave shape approximating. Two constraints namely power condition and zero-crossing-shift condition are developed to ensure the wave shape approximation of i_o and v_o, respectively. A third phase-locked condition is used to constrain the time interval $\Delta t_{\rm ps}$ in the phase-locked loop control as in Fig. 5(b). Finally, the results of n, C_p, L_s, and L_m are attained by solving the equations in the three constraint conditions.

It should be noted that a linear DBD model is adopted in the second step for two reasons. First, the parameter design in this study needs to decouple and separately analyze the third harmonic component, which is difficult for a circuit with the nonlinear DBD model. Thus, for the convenience of circuit decoupling analysis, Fourier transform is employed to establish the linear DBD models composed of resistor and capacitor at f_s and $3f_s$. Second, the parallel-series resonant tank in Fig. 5(a) has a nonlinear part and up to five resonant elements. If the accurate piecewise mathematical approaches in [3], [4], and [22]

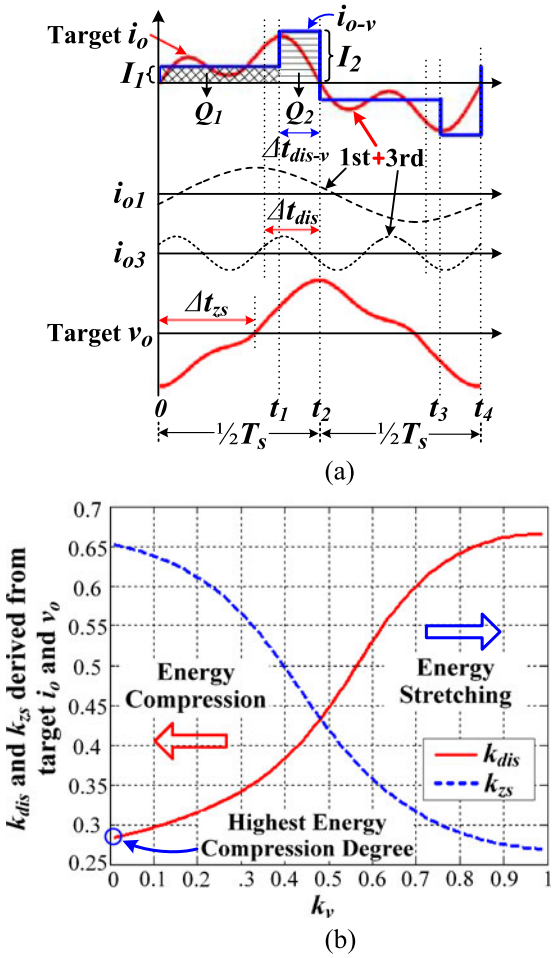

Fig. 7. Rectangular current estimation: (a) waveforms of i_{o-v} and target i_o, v_o and (b) relationship among k_v, $k_{\rm dis}$ and k_{zs} derived from target i_o, v_o.

are used, the calculation difficulty would be greatly increased. The linear model avoids the complex piecewise analysis in the second step, which simplifies the calculation but does not affect the accuracy.

A. Step I: Estimation Through a Piecewise Rectangular Current

As mentioned previously, this step is intended to define a piecewise rectangular current i_{o-v} and estimate the desired wave shapes of i_o and v_o (wave shape targets) according to the given parameters: $C_d, C_g, V_T, P_{o-\rm av}, f_s$.

1) Definition of a Piecewise Rectangular Current i_{o-v}: The waveform of current i_{o-v} in one switching period T_s is shown in Fig. 7(a), which has two different current amplitudes for different time intervals. During the interval from *0* to t_1, or from t_2 to t_3, the current amplitude is I_1. The interval from t_1 to t_2, or from t_3 to t_4 is called the virtual discharge time $\Delta t_{{\rm dis}-v}$ as marked in Fig. 7(a). Another current amplitude I_2 appears during this virtual discharge. A virtual discharge-time-ratio k_v, defined as the ratio of $\Delta t_{{\rm dis}-v}$ to $1/2T_s$, is utilized to determine the instants t_1 and t_3. At a given period $T_s(=1/f_s)$, the various instants of i_{o-v} in Fig. 7(a) are calculated as follows. k_v can be set to any value between 0 and 1

$$\begin{cases} t_1 = \dfrac{T_s}{2} - \Delta t_{{\rm dis}-v} = \dfrac{T_s}{2} - \dfrac{T_s}{2}k_v = \dfrac{1-k_v}{2f_s} \\ t_2 = \dfrac{T_s}{2} = \dfrac{1}{2f_s} \\ t_3 = T_s - \Delta t_{{\rm dis}-v} = T_s - \dfrac{T_s}{2}k_v = \dfrac{2-k_v}{2f_s} \\ t_4 = T_s = \dfrac{1}{f_s} \end{cases}. \quad (1)$$

The physical meaning of i_{o-v} is explained as follows. i_{o-v} is assumed to be injected into the nonlinear DBD model in Fig. 1(a). The current level I_1 during the interval from *0* to t_1 charges v_{Cg} and changes it from $-V_T$ to $+V_T$ as at the charge stage in Fig. 1(c), and in the meantime, an electric charge Q_1 flows through the DBD model. Q_1 is only determined by C_g and the gap voltage increment $2V_T$ during this stage [3] as in (2). The current level I_2 during $\Delta t_{{\rm dis}-v}$ from t_1 to t_2 produces the discharge with v_{Cg} clamped to V_T as at the discharge stage in Fig. 1(d), and in the meantime, an electric charge Q_2 flows through the DBD model. The average power consumed by injecting i_{o-v} is the given power $P_{o-\rm av}$. Q_1 and Q_2 can be represented by the areas of shaded parts below the i_{o-v} waveform marked in Fig. 7(a). Thus, Q_1 and Q_2 are expressed as the following two equations in (2), from which I_1 and I_2 can also be calculated as

$$\begin{cases} \int_0^{t_1} I_1 dt = Q_1 = 2V_T C_g \Rightarrow I_1 = \dfrac{4V_T f_s C_g}{1-k_v} \\ \int_{t_1}^{t_2} I_2 dt = Q_2 = \dfrac{P_{o-\rm av}}{2V_T f_s} \Rightarrow I_2 = \dfrac{P_{o-\rm av}}{V_T k_v} \end{cases}. \quad (2)$$

From (1) and (2), i_{o-v} can be expressed as below. The coefficient k_v in a range from 0 to 1 is the freedom degree of the wave shape of i_{o-v}

$$i_{o-v}(t) = \begin{cases} I_1 = \dfrac{4V_T f_s C_g}{1-k_v} & 0 \le t < \dfrac{1-k_v}{2f_s} \\ I_2 = \dfrac{P_{o-\rm av}}{V_T k_v} & \dfrac{1-k_v}{2f_s} \le t < \dfrac{1}{2f_s} \\ -I_1 = -\dfrac{4V_T f_s C_g}{1-k_v} & \dfrac{1}{2f_s} \le t < \dfrac{2-k_v}{2f_s} \\ -I_2 = -\dfrac{P_{o-\rm av}}{V_T k_v} & \dfrac{2-k_v}{2f_s} \le t < \dfrac{1}{f_s} \end{cases}. \quad (3)$$

2) Estimation of the Current and Voltage Wave Shape Targets: The desired wave shapes estimated below are called the wave shape targets. Fourier analysis is adopted to calculate the fundamental component i_{o1} and the third harmonic component i_{o3} of i_{o-v}, which are drawn by two dashed lines in Fig. 7(a). These two currents are called target i_{o1} and target i_{o3}, respectively. The sum of these two current components $(i_{o1}+i_{o3})$ is called the target i_o, which gives the target wave shape of the output current as shown in Fig. 7(a).

Injecting the target i_o into the DBD load produces a target voltage v_o across the load, which gives the target wave shape of the output voltage and is also shown in Fig. 7(a). So far, the wave shapes of the target i_o and v_o have been estimated from the rectangular current i_{o-v} at a certain k_v.

3) Wave Shape Targets at the Highest Energy Compression Degree: From the wave shapes of target i_o and v_o at a given k_v, the two time intervals $\Delta t_{\rm dis}$ and $\Delta t_{\rm zs}$ in Fig. 7(a) can be derived using MATLAB. Then, the values of coefficients $k_{\rm dis}$ and $k_{\rm zs}$ at the given k_v can be calculated. Varying k_v from 0 to 1 gives different sets of $k_{\rm dis}$ and $k_{\rm zs}$ values. The relationships among k_v, $k_{\rm dis}$, and $k_{\rm zs}$ are described by two curves in Fig. 7(b), which is used to find the target wave shapes at the highest energy compression degree. In Fig. 7(b), $k_{\rm dis}$ reaches the minimum or λ reaches the maximum when k_v infinitely approaches $0 (k_v \rightarrow 0)$. Thus, the wave shapes in Fig. 7(a) give the target wave shapes at the highest energy compression degree if $k_v \rightarrow 0$ or $\Delta t_{{\rm dis}-v} \rightarrow 0$.

As defined in Section III, the coefficient $k_{\rm zs}$ reflects the wave shape correlation between i_o and v_o from the perspective of zero crossing point difference. Thus, k_v and $k_{\rm zs}$ serve as the wave shape freedom degrees of target i_o and target v_o, respectively.

B. Step II: Circuit Superposition and Wave Shape Approximating

In this step, three substeps will be performed in turn. First, two linear equivalent subcircuits operating at f_s and $3f_s$ are established by linearizing the DBD model in Fig. 1. And then, these two subcircuits are superposed linearly to generate the synthesized wave shapes of i_o and v_o. Finally, the design results of n, C_p, L_s, and L_m are attained by approximating these superposed wave shapes to the wave shape targets in Step I under three constraint conditions.

1) Establishment of Two Linear Subcircuits Operating at f_s and $3f_s$: A resistor in series with a capacitor is used to model the nonlinear rectifying part of the resonant converter with excellent accuracy in a method of RCFHA [25]. Similarly, RCFHA can also be employed to model the combination of C_g, V_T, and $D_{o1} \sim D_{o4}$ of the DBD model's nonlinear part (excluding C_d) [26]. Thus, by combining C_d and the equivalent capacitor in RCFHA, the whole DBD load can be modeled by the series combination of a resistor and a capacitor as in [26]. The calculation method in [26] is employed at both f_s and $3f_s$ in this step. Then, the DBD equivalent resistance $R_{\rm eq1}$ at f_s and the equivalent capacitances $C_{\rm eq1}, C_{\rm eq3}$ at $f_s, 3f_s$ can be calculated. $R_{\rm eq1}$ represents the average real power consumption at f_s. The equivalent capacitance $R_{\rm eq3}$ at $3f_s$ is not listed here because the power consumption at $3f_s$ is neglected in the following analysis. As a result, the current-fed parallel-series resonant converter in Fig. 5(a) is decoupled into two linear subcircuits operating at f_s and $3f_s$ in Fig. 8. The fundamental component $i_{\rm exc1}$ of square-wave $i_{\rm exc}$ in Fig. 5(b) is fed into the resonant tank in the fundamental equivalent circuit in Fig. 8(a). The third harmonic equivalent circuit in Fig. 8(b) has no input current as the effect of the third harmonic component of input current $i_{\rm exc}$ is neglected. Another current source with the amplitude and phase

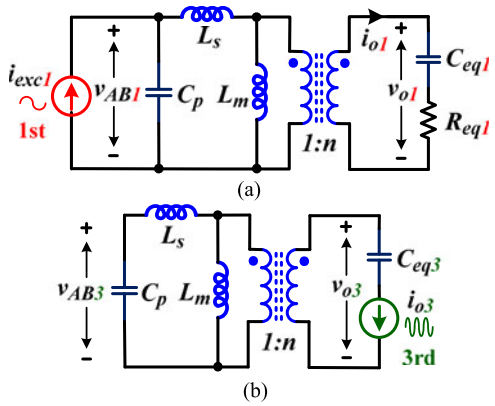

Fig. 8. Two linear equivalent sub-circuits derived from current-fed parallel-series resonant converter: (a) fundamental circuit and (b) third harmonic circuit.

of the target current i_{o3} in Step I is injected into the load as in Fig. 8(b), which represents the third harmonic circulating current explained in Section III. As shown in Fig. 5, the rated dc current $I_{\rm dc}$ can be theoretically calculated by using the rated $P_{o-{\rm av}}$, grid rectified voltage $V_{\rm rec}$, and maximum buck circuit duty cycle $D_{\rm buck-max}$ (i.e., rated $I_{\rm dc} = P_{o-{\rm av}}/(V_{\rm rec} D_{\rm buck-max})$) as in [22]. From Fourier analysis, the amplitude of $i_{\rm exc1}$ in Fig. 8(a) is calculated to be $4/p$ times as large as this rated $I_{\rm dc}$. Thus, two subcircuits have been established with four unsolved parameters: n, C_p, L_s, and L_m.

2) Linear Superposition of Two Subcircuits: The linear superposition means that the corresponding variables in the two linear equivalent subcircuits in Fig. 8 are added to express a superposed wave shape

$$x(n, C_p, L_s, L_m, t) = x_1(n, C_p, L_s, L_m, t) + x_3(n, C_p, L_s, L_m, t) \quad (4)$$

where x represents any superposed circuit variable like i_o, v_o, and $v_{\rm AB}$. And x_1 and x_3 represent the variables in the fundamental and third harmonic subcircuits, respectively. x, x_1, and x_3 are all functions of the four unsolved parameters: n, C_p, L_s, and L_m.

3) Wave Shape Approximation Under Three Constraints: There are three constraint conditions to fulfill in the wave shape approximating. The three constraints will be verified through the wave shape agreement between the superposed waves in Step II and target waves in Step I in Section V.

1) *Power condition*. Since the third harmonic subcircuit in Fig. 8(b) is assumed to have no real power consumption, the output power $P_{o-{\rm av}}$ can be calculated as

$$P_{o-{\rm av}} = \frac{I_{o1}(n, C_p, L_s, L_m)^2 R_{\rm eq1}}{2} \quad (5)$$

where $I_{o1}(n, C_p, L_s, L_m)$ is the amplitude of the fundamental subcircuit output current $i_{o1}(n, C_p, L_s, L_m, t)$ in Fig. 8(a). This condition makes $i_{o1}(n, C_p, L_s, L_m, t)$ in Step II approximate its target i_{o1} in Step I. The superposed $i_o(n, C_p, L_s, L_m, t)$ is the sum of this $i_{o1}(n, C_p, L_s, L_m, t)$ and the target i_{o3} in Step I as stated previously. Thus, the superposed $i_o(n, C_p, L_s, L_m, t)$ in

TABLE I
CONVERTER SPECIFICATIONS AND DBD PARAMETERS

Parameter	Value
Grid RMS Voltage $V_{\rm in}$	220 V
Grid Frequency $f_{\rm in}$	50 Hz
Rated Rectified Voltage $V_{\rm rec}$	310 V
Rated Output Power $P_{o-{\rm av}}$	350 W
Rated Switching Frequency f_s	30 kHz
Dielectric Barrier Capacitance C_d	0.155 nF
Air Gap Capacitance C_g	0.256 nF
Discharge Maintaining Voltage V_T	3300 V

Step II approximates its target $i_o(t)$ that equals the sum of target i_{o1} and target i_{o3} in Step I.

2) *Zero-crossing-shift condition*. In this condition, the coefficient $k_{\rm zs}$ is used to ensure the wave shape approximation of v_o. As mentioned in Step I, $k_{\rm zs}$ represents the freedom degree of the wave shape target of v_o. So the approximation of the $k_{\rm zs}$ value reflects the approximation of the v_o wave shape. In other words, the value of $k_{\rm zs}(n, C_p, L_s, L_m)$ deduced from the superposed $i_o(n, C_p, L_s, L_m, t)$ and $v_o(n, C_p, L_s, L_m, t)$ in Step II should be equal to the value of $k_{\rm zs}(C_d, C_g, V_T, P_{o-av}, f_s, k_v)$ calculated from the target wave shapes in Step I:

$$k_{\rm zs}(n, C_p, L_s, L_m) = k_{\rm zs}(C_d, C_g, V_T, P_{o-{\rm av}}, f_s, k_v). \tag{6}$$

3) *Phase-locked condition*. This condition is developed to ensure the small fixed time $\Delta t_{\rm ps}$ between the zero crossing points of the superposed $v_{\rm AB}$ and $i_{\rm exc1}$ due to the phase-locked loop technique. If the sinusoidal $i_{\rm exc1}$ in Fig. 8(a) is expressed as $(4/\pi I_{\rm dc})\sin(w_s t + \theta)$, the moment of the zero crossing point of $i_{\rm exc1}$ is calculated as $-\theta/w_s$. Then, the moment of the zero crossing point of superposed $v_{\rm AB}(n, C_p, L_s, L_m, t)$ is calculated to be $-\theta/w_s - \Delta t_{\rm ps}$. Thus, the zero crossing point of $v_{\rm AB}(n, C_p, L_s, L_m, t)$ can be expressed as the following equation:

$$v_{\rm AB}(n, C_p, L_s, L_m, -\theta/w_s - \Delta t_{\rm ps}) = 0 \tag{7}$$

where w_s is the angular frequency, $w_s = 2\pi f_s$.

The design results of n, C_p, L_s, and L_m can be obtained by solving (5), (6), and (7). All the solutions can be plotted as curves to reveal the relationship of these four variables. The specifications and DBD load parameters at the rated power are described in Table I, which are the same as for the DCM configuration in Fig. 2. About 30 kHz is a common and typical frequency for DBD surface treatment (median in 10–50 kHz range [10]). $k_{\rm dis}$ reaches 0.285 when $k_v \to 0$. Parameters $R_{\rm eq1}, C_{\rm eq1}, C_{\rm eq3}$ are also calculated at $k_v \to 0$.

By solving (5), (6), and (7), three curves can be drawn on the coordinate planes of (C_p, n), (L_s, n), and (L_m, n) in Fig. 9(a) and (b) by using MATLAB, with the turns ratio n as the independent variable. L_s and L_m in Fig. 9(b) are realized by using the air gap inductors. The values of L_s and L_m are adjusted by changing the air gaps. Fig. 9(c) plots the peak values of $v_{\rm AB}$ at different n values, which determines the voltage stresses on the active switches and capacitor C_p. Fig. 9(d) gives the root-mean-square

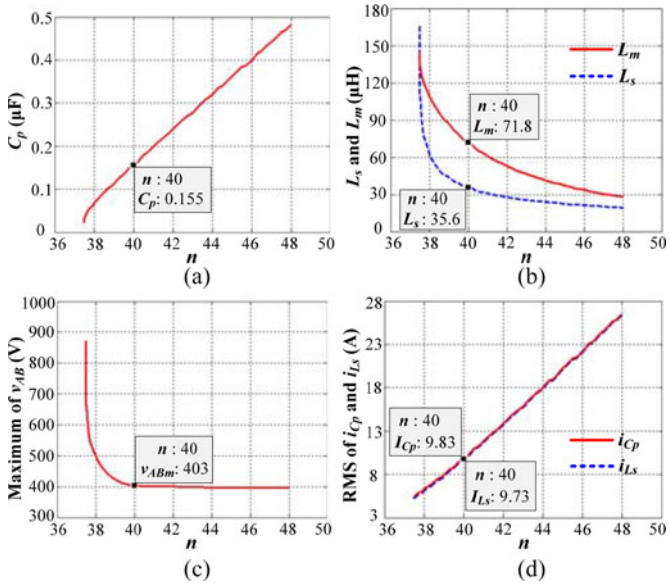

Fig. 9. Curves for design optimization: (a) C_p versus n curve; (b) L_s and L_m versus n curves; (c) maximum $v_{\rm AB}$ versus n curve; and (d) RMS of i_{Cp} and i_{Ls} versus n curves.

TABLE II
OPTIMAL DESIGN RESULTS OF PARALLEL-SERIES RESONANT TANK

Parameter	Value
Turns Ratio n	40
Parallel Capacitance C_p	0.155 μF
Series Inductance L_s	35.6 μH
Magnetizing Inductance L_m	71.8 μH

TABLE III
DEVICES USED IN TESTED PROTOTYPE

Parameter	Value
Bridge Rectifier (D_r)	KBPC1510
Buck Active Switch (S_c)	IKW15T120
H-bridge Active Switches (S_1–S_4)	IKW15N120H3
Freewheeling Diode (D_c) and Reverse-voltage Blocking Diodes (D_{s1}–D_{s4})	IDP18E120
Electrolytic Filter Capacitors (C_f)	1500 μF
dc Link Inductor ($L_{\rm dc}$)	4 mH

(RMS) currents through C_p and L_s at different n, which affects the capacitor selection and transformer winding losses.

With n decreased, C_p reduces but L_s and L_m increase rapidly. A smaller volume or lower cost capacitor are accompanied by a larger magnetic core or more turns for the inductor. So the inductance and capacitance selection goals are in conflict. As n reduces, the $v_{\rm AB}$ peak first increases slowly from 400 V and, then, rises sharply toward 900 V. However, i_{Cp} and i_{Ls} reduces almost linearly as n decreases. So the voltage and current stresses contradict. To make both the voltage stress (peak value of $v_{\rm AB}$) and current stress (RMS of i_{Cp} or i_{Ls}) as low as possible, the optimal value of n is selected at the point in Fig. 9(c) where the peak value of $v_{\rm AB}$ just starts to rise rapidly with the decrease of n. The optimal results are marked in Fig. 9 and listed in Table II.

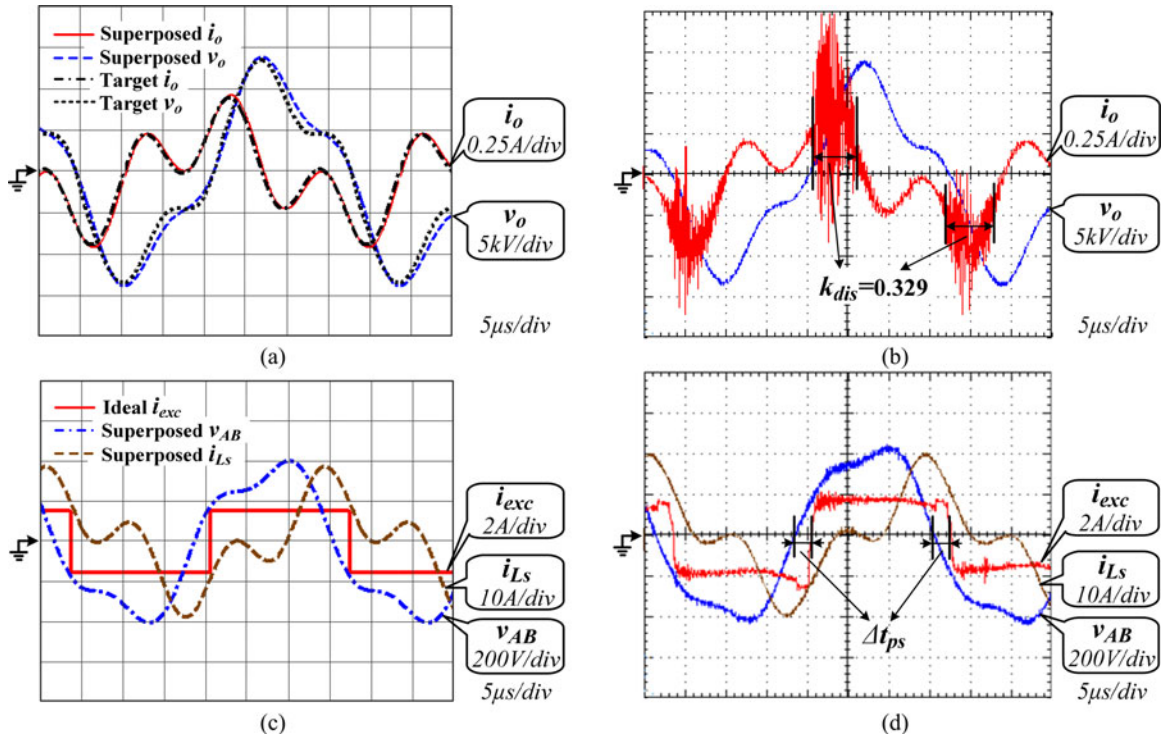

Fig. 10. Theoretical and experimental waveforms with $L_s = 35.6\,\mu$H: (a) target i_o, v_o waves and superposed i_o, v_o waves; (b) experimental i_o, v_o waves; (c) ideal $i_{\rm exc}$ wave and superposed $v_{\rm AB}, i_{Ls}$ waves; and (d) experimental $i_{\rm exc}$, $v_{\rm AB}$ and i_{Ls} waves.

V. Experimental Results

To verify the RCFTHA and the effectiveness of the third harmonic circulating current, an experimental prototype was built by using the given parameters in Table I and the design results in Table II. The DBD load used here is the same as that in the DCM experiments in Section II. Other devices are described in Table III. The buck circuit operates at 16 kHz, which avoids the audible noises and lowers the buck circuit's switching loss simultaneously. The voltage and current on the transformer primary side are measured by the voltage probe P5200A and current probe CWT015, respectively. The voltage and current on the secondary side are measured by the high voltage probe P6015A and a 20 Ω sense resistor, respectively. The phase-shifts induced by these probes are negligible. A Tektronix TPS2024 digital oscilloscope is used to record the voltage and current waveforms.

Fig. 10(a) and (c) present the theoretical waveforms at the rated power with the parameters in Table II by using MATLAB: the target i_o, v_o waves estimated from the rectangular current i_{o-v} at $k_v \to 0$, the ideal $i_{\rm exc}$ square-wave and the superposed $i_o, v_o, v_{\rm AB}, i_{Ls}$ waves from the linear superposition. In Fig. 10(a), the superposed i_o and v_o wave shapes are coincident with their target wave shapes, which verifies the accuracy of the power and zero-crossing-shift constraint conditions in the RCFTHA. Fig. 10(b) and (d) illustrates the steady-state experimental waveforms of $i_o, v_o, v_{\rm AB}, i_{Ls}$, and $i_{\rm exc}$ at the rated power. $i_o, v_o, v_{\rm AB}$, and i_{Ls} contain obvious third harmonic components, which proves the existence of third harmonic circulating current and the achievement of two resonances at f_s and $3f_s$ in the resonant tank as in Fig. 4(b). Compared to the target and superposed waveforms, the experimental waveforms have the same shapes except the microdischarge currents on i_o and the ripple current on $i_{\rm exc}$, which verifies the rationality and accuracy of the wave shape estimation, circuit superposition, and wave shape approximation method in the RCFTHA. The shape agreement is also a validation of the two assumptions made earlier in Section IV: the neglects of the third harmonic excitation current impact and the power consumption at $3f_s$. The actual $k_{\rm dis}$ in Fig. 10(b) is measured to be 0.329 and close to its target $k_{\rm dis}$ of 0.285, which points out the RCFTHA effectiveness in the discharge-time-ratio design. So the actual highest energy compression degree is calculated to be 1.61 according to the $k_{\rm dis-sin}$ of 0.530 shown in Fig. 2(d). The switching frequency f_s and time interval $\Delta t_{\rm ps}$ in Fig. 10(d) are measured to respectively equal the set values of 30 kHz and 2 μs, which proves the effectiveness of the phase-locked constraint condition. In addition, i_o has a wave shape and a discharge-time-ratio similar to those in Fig. 2(b), verifying that the third harmonic load current achieves the energy compression like the DCM. However, the peak current through the power devices is only one-tenth of that in the DCM shown in Fig. 2(c).

Based on the given parameters in Table I, other sets of parameters can be found out to realize other different wave shapes and $k_{\rm dis}$ values by selecting other k_v values, which have the same n, C_p and L_m as those in Table II but different L_s. Figs. 11 and 12 give the theoretical and experimental waveforms at

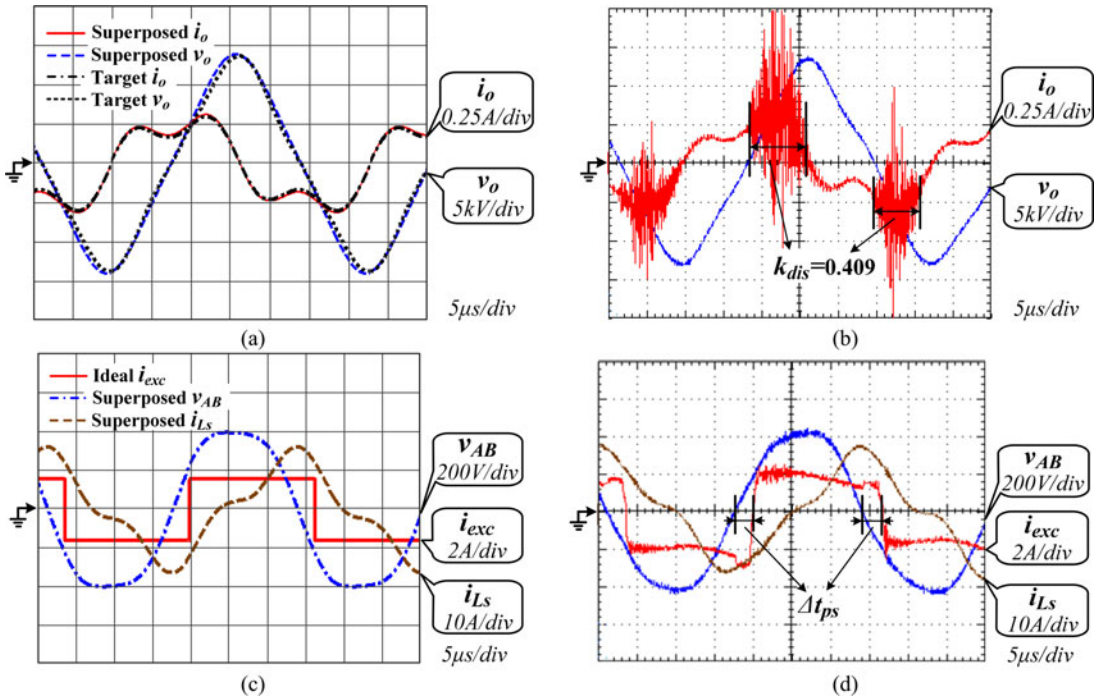

Fig. 11. Theoretical and experimental waveforms with $L_s = 29.0\,\mu$H: (a) target i_o, v_o waves and superposed i_o, v_o waves; (b) experimental i_o, v_o waves; (c) ideal $i_{\rm exc}$ wave and superposed $v_{\rm AB}, i_{Ls}$ waves; and (d) experimental $i_{\rm exc}, v_{\rm AB}$ and i_{Ls} waves.

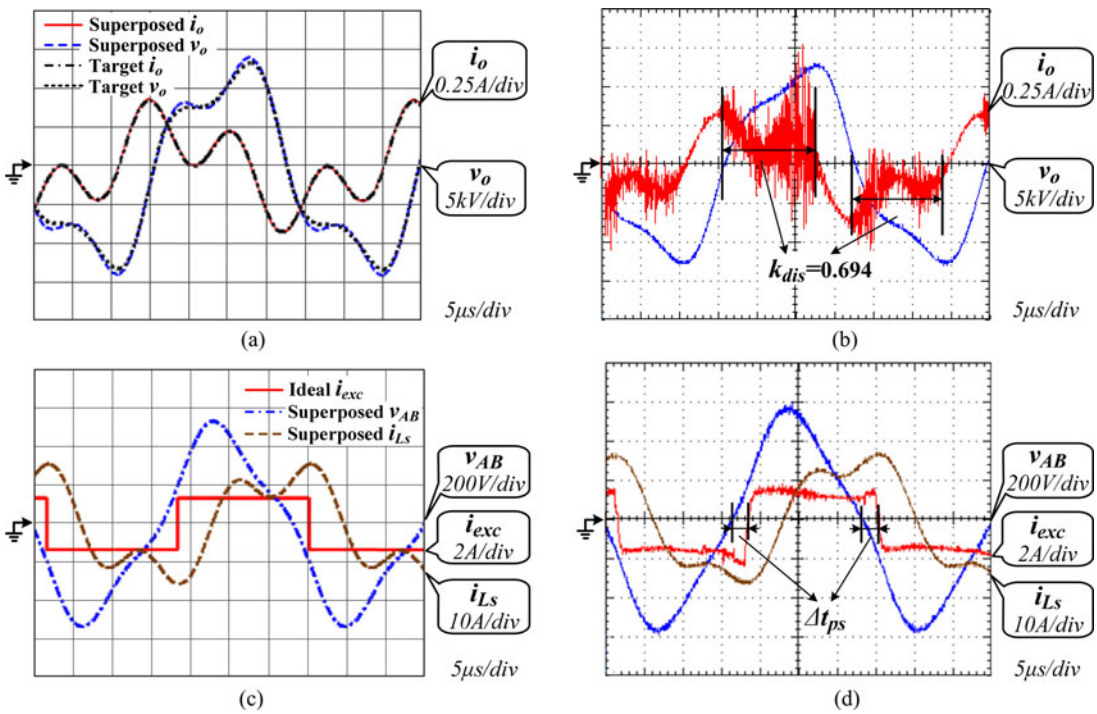

Fig. 12. Theoretical and experimental waveforms with $L_s = 49.0\,\mu$H: (a) target i_o, v_o waves and superposed i_o, v_o waves; (b) experimental i_o, v_o waves; (c) ideal $i_{\rm exc}$ wave and superposed $v_{\rm AB}, i_{Ls}$ waves; and (d) experimental $i_{\rm exc}, v_{\rm AB}$ and i_{Ls} waves.

the rated power when $L_{\rm s}$ is, respectively, changed to 29.0 and 49.0 μH: the target i_o, v_o waves, the ideal $i_{\rm exc}$ square-wave, and the superposed $i_o, v_o, v_{\rm AB}, i_{Ls}$ waves. A $k_{\rm dis}$ of 0.409 is achieved when L_s is 29.0 μH in Fig. 11, where the energy compression degree is 1.30. If L_s is changed to 49.0 μH, the actual $k_{\rm dis}$ becomes 0.694 in Fig. 12, realizing an energy compression degree of 0.76. So the energy stretching can also be realized through the third harmonic circulating current. From the similarity between the theoretical and experimental waveforms, the same conclusions as in Fig. 10 can be drawn, such as the third

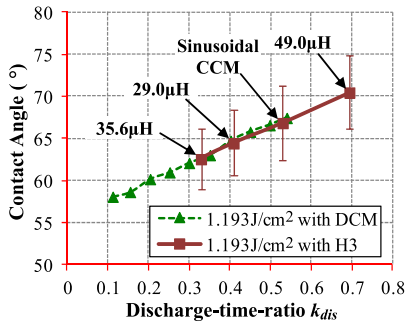

Fig. 13. Contact angles measured with different series inductance L_s values at the plasma dose density of 1.193 J/cm^2.

harmonic circulating current existence, the linear superposition effectiveness and the RCFTHA accuracy.

From Figs. 10–12, it is verified that the wave shape depends on the resonant parameter selection and is not related to the circuit control. In the above three cases, the peak current through the power devices is around 2 A and close to that of sinusoidal CCM shown in Fig. 2(e). The third harmonic circulating current is verified not to increase the inverter current stress.

To verify the superior treatment performance with the third harmonic (H3) circulating current, the above three groups of experimental waveforms with three different L_s values were applied in the treatment of the PE films. As a comparison, the sinusoidal CCM case was also realized on this prototype by removing the inductor L_{s1} and turning the resonant network into the parallel structure as in [22]. C_p was changed from 0.155 to 0.2 μF to maintain the resonant frequency around 30 kHz. The correspondence between the dose density and power is the same as that in the DCM configuration in Section II. Fig. 13(a) shows the water contact angles measured with three different L_s values at the rated power (at the dose density of 1.193 J/cm^2). Compared with the sinusoidal case, the energy compression ($\lambda > 0$) with the L_s values of 35.6 and 29.0 μH leads to smaller contact angles, while the energy stretching ($\lambda < 0$) with the L_s value of 49.0 μH results in a larger contact angle. The greatest contact angle decrease of 6.4% is achieved at the highest energy compression degree with the optimal design results in Table II. The contact angles measured in the DCM at the dose density of 1.193 J/cm^2 in Fig. 2(d) is also shown in Fig. 13 to compare with the results of the third harmonic current circulation. Despite occupying different $k_{\rm dis}$ ranges, the two lines in Fig. 13 have similar slopes, and they almost coincide completely when $k_{\rm dis}$ is between 0.33 and 0.53. Thus, the relationship between the contact angle and the discharge-time-ratio obtained by using the third harmonic current circulation conforms to the law about energy compression illustrated in Section II.

VI. Conclusion

This paper presents an energy compression technique in the DBD surface treatment applications, which is implemented by generating a third harmonic circulating current within the resonant tank in the current-fed parallel-series resonant converter. The wave shape with third harmonic circulating current needs no special active control. Furthermore, a RCFTHA method has been introduced to design the resonant parameters by describing the current-fed parallel-series resonant converter as the linear superposition of two equivalent circuits at the fundamental and third harmonic frequencies, respectively. Finally, the RCFTHA accuracy and the energy compression effectiveness have been verified by experimentation on a 350-W prototype. Compared with the sinusoidal CCM case, the third harmonic current circulation method improves the surface wettability by 6.4% with the highest energy compression degree of 1.61 and a dose density of 1.193 J/cm^2. Meanwhile, the inverter current stress is close to that in sinusoidal CCM and only one-tenth of that in DCM at the same energy compression degree. It can be concluded that the resonant converter with the third harmonic circulating current is a viable candidate for industrial DBD applications.

References

[1] M. Amjad, Z. Salam, M. Facta, and S. Mekhilef, "Analysis and implementation of transformerless LCL resonant power supply for ozone generation," *IEEE Trans. Power Electron.*, vol. 28, no. 2, pp. 650–660, Feb. 2013.

[2] X. Bonnin, J. Brandelero, N. Videau, H. Piquet, and T. Meynard, "A high voltage high frequency resonant inverter for supplying DBD devices with short discharge current pulses," *IEEE Trans. Power Electron.*, vol. 29, no. 8, pp. 4261–4269, Aug. 2014.

[3] T. Guo, S. Hao, C. Zhang, J. Liu, Y. Deng, and X. He, "Analysis and design of pulse frequency modulation discontinuous-current-mode dielectric barrier corona discharge with constant applied electrode voltage," *IET Power Electron.*, vol. 7, no. 11, pp. 2857–2869, 2014.

[4] D. Florez, R. Diez, and H. Piquet, "DCM-Operated series-resonant inverter for the supply of DBD excimer lamps," *IEEE Trans. Ind. Appl.*, vol. 50, no. 1, pp. 86–93, Jan./Feb. 2014.

[5] N. Burany, L. Huber, and P. Pejovic, "Corona discharge surface treater without high voltage transformer," *IEEE Trans. Power Electron.*, vol. 23, no. 2, pp. 993–1002, Mar. 2008.

[6] C. Wang and X. He, "Preparation of hydrophobic coating on glass surface by dielectric barrier discharge using a 16 kHz power supply," *Appl. Surf. Sci.*, vol. 252, no. 23, pp. 8348–8351, Sep. 2006.

[7] C. Zhang, T. Shao, K. Long, Y. Yu, J. Wang, D. Zhang, P. Yan, and Y. Zhou, "Surface treatment of polyethylene terephthalate films using DBD excited by repetitive unipolar nanosecond pulses in air at atmospheric pressure," *IEEE Trans. Plasma Sci.*, vol. 38, no. 6, pp. 1517–1526, Jun. 2010.

[8] Z. Fang, J. Lin, H. Yang, Y. Qiu, and E. Kuffel, "Polyethylene terephthalate surface modification by filamentary and homogeneous dielectric barrier discharges in air," *IEEE Trans. Plasma Sci.*, vol. 37, no. 5, pp. 659–667, May 2009.

[9] N. De Geyter, R. Morent, and C. Leys, "Pressure dependence of helium DBD plasma penetration into textile layers," *IEEE Trans. Plasma Sci.*, vol. 36, no. 4, pp. 1308–1309, Aug. 2008.

[10] U. Kogelschatz, "Dielectric-barrier discharges: Their history, discharge physics, and industrial applications," *Plasma Chem. Plasma Process.*, vol. 23, no. 1, pp. 1–46, Mar. 2003.

[11] C. Jia, P. Chen, W. Liu, B. Li, and Q. Wang, "Surface treatment of aramid fiber by air dielectric barrier discharge plasma at atmospheric pressure," *Appl. Surf. Sci.*, vol. 257, no. 9, pp. 4165–4170, Feb. 2011.

[12] Z. Fang, X. Qiu, Y. Qiu, and E. Kuffel, "Dielectric barrier discharge in atmospheric air for glass-surface treatment to enhance hydrophobicity," *IEEE Trans. Plasma Sci.*, vol. 34, no. 4, pp. 1216–1222, Aug. 2006.

[13] C. Liu, N. M. D. Brown, and B. J. Meenan, "Statistical analysis of the effect of dielectric barrier discharge (DBD) operating parameters on the surface processing of poly (methylmethacrylate) film," *Surf. Sci.*, vol. 575, no. 3, pp. 273–286, Feb. 2005.

[14] A. L. Santos, E. C. Botelho, K. G. Kostov, P. A. P. Nascente, and L. L. G. Da Silva, "Atmospheric plasma treatment of carbon fibers for enhancement of their adhesion properties," *IEEE Trans. Plasma Sci.*, vol. 41, no. 2, pp. 319–324, Feb. 2013.

[15] S. Hao, C. Zhang, T. Guo, X. Liu, S. Hu, J. Liu, and X. He, "A current-fed asymmetric LLCC resonant converter for DBD applications," in *Proc. IEEE Annu. Appl. Power Electron. Conf. Expo.*, 2014, pp. 873–878.
[16] S. Bae, A. Kwasinski, M. M. Flynn, and R. E. Hebner, "High-power pulse generator with flexible output pattern," *IEEE Trans. Power Electron.*, vol. 25, no. 7, pp. 1675–1684, Jul. 2010.
[17] K. Kyrberg, H. Guldner, A. Rupp, and O. Schallmoser, "Half-Bridge and full- bridge choke converter concepts for the pulsed operation of large dielectric barrier discharge lamps," *IEEE Trans. Power Electron.*, vol. 22, no. 3, pp. 926–933, May 2007.
[18] T. Shao, D. Zhang, Y. Yu, C. Zhang, J. Wang, P. Yan, and Y. Zhou, "A compact repetitive unipolar nanosecond-pulse generator for dielectric barrier discharge application," *IEEE Trans. Plasma Sci.*, vol. 38, no. 7, pp. 1651–1655, Jul. 2010.
[19] Y. Liu and X. He, "PDM and PFM hybrid control of a series-resonant inverter for corona surface treatment," *IEE Proc.-Electr. Power Appl.*, vol. 152, no. 6, pp. 1445–1450, Nov. 2005.
[20] V. Kinnares and P. Hothongkham, "Circuit analysis and modeling of a phase-shifted pulsewidth modulation full-bridge-inverter-fed ozone generator with constant applied electrode voltage," *IEEE Trans. Power Electron.*, vol. 25, no. 7, pp. 1739–1752, Jul. 2010.
[21] T. Liang, R. Chen, and J. Chen, "Current-Fed parallel-resonant DC-AC inverter for cold-cathode fluorescent lamps with zero-current switching," *IEEE Trans. Power Electron.*, vol. 23, no. 4, pp. 2206–2210, Jul. 2008.
[22] L. Chang, T. Guo, J. Liu, C. Zhang, Y. Deng, and X. He, "Analysis and design of a current-source CLCC resonant converter for DBD applications," *IEEE Trans. Power Electron.*, vol. 29, no. 4, pp. 1610–1621, Apr. 2014.
[23] A. J. Gilbert, C. M. Bingham, D. A. Stone, and M. P. Foster, "Normalized analysis and design of LCC resonant converters," *IEEE Trans. Power Electron.*, vol. 22, no. 6, pp. 2386–2402, Nov. 2007.
[24] R. L. Steigerwald, "A comparison of half-bridge resonant converter topologies," *IEEE Trans. Power Electron.*, vol. 3, no. 2, pp. 174–182, Apr. 1988.
[25] N. Shafiei, M. Pahlevaninezhad, H. Farzanehfard, A. Bakhshai, and P. Jain, "Analysis of a fifth-order resonant converter for high-voltage DC power supplies," *IEEE Trans. Power Electron.*, vol. 28, no. 1, pp. 85–100, Jan. 2013.
[26] T. Guo, X. Liu, S. Hao, C. Zhang, and X. He, "Analysis and design of pulse frequency modulation dielectric barrier discharge for low power applications," *Frontiers Inf. Technol. Electron. Eng.*, vol. 16, no. 3, pp. 249–258, Mar. 2015.
[27] J. M. Espi-Huerta, E. J. D. G. Santamaria, R. G. Gil, and J. Castello-Moreno, "Design of the L-LC resonant inverter for induction heating based on its equivalent SRI," *IEEE Trans. Ind. Electron.*, vol. 54, no. 6, pp. 3178–3187, Dec. 2007.

Shiqiang Hao received the B.Sc. and M.Sc. degrees from the College of Automation, Wuhan University of Technology, Wuhan, China, in 2009 and 2012, respectively. He is currently working toward the Ph.D. degree in the College of Electrical Engineering, Zhejiang University, Hangzhou, China.

His research interests include topologies and control of resonant power conversion, and high voltage converters in industrial applications of low temperature plasma.

Xingliang Liu was born in 1990 in Shandong, China. He received the B.S. degree from the Department of Electrical Engineering, Shandong University, Jinan, China, in 2012. He is currently working toward the Ph.D. degree in the College of Electrical Engineering, Zhejiang University.

His research interests include high voltage resonant converters and pulse generators in the applications of nonequilibrium plasma.

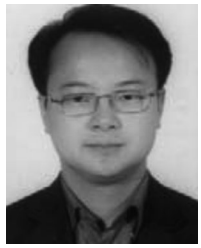

Wuhua Li (M'09) received the B.Sc. and Ph.D. degrees in applied power electronics and electrical engineering from Zhejiang University, Hangzhou, China, in 2002 and 2008, respectively.

From 2004 to 2005, he was a Research Intern, and from 2007 to 2008, a Research Assistant in GE Global Research Center, Shanghai, China. From 2008 to 2010, he joined the College of Electrical Engineering, Zhejiang University as a Postdoctor. In 2010, he was promoted as an Associate Professor. Since 2013, he has been a Full Professor at Zhejiang University. From 2010 to 2011, he was a Ryerson University Postdoctoral Fellow with the Department of Electrical and Computer Engineering, Ryerson University, Toronto, ON, Canada. His research interests include high power devices, advanced power converters, and operation optimization for renewable energy-based power systems. He has published more than 100 peer-reviewed technical papers and holds more than 30 issued/pending patents.

Dr. Li received the 2011 TOP TEN Excellent Young Staff Award and the 2012 Distinguished Young Scholar from Zhejiang University, the 2012 Outstanding Young Researcher Award from Zhejiang Province, the 2012 Delta Young Scholar from Delta Environmental & Educational Foundation, and the 2012 National Outstanding Young Scholar due to his excellent teaching and research contributions. He received four Scientific and Technological Achievements Awards from Zhejiang Provincial Government and the State Educational Ministry of China in 2009, 2011, and 2014, respectively.

Yan Deng received the B.E.E. degree from the Department of Electrical Engineering, Zhejiang University, Hangzhou, China, in 1994, and the Ph.D. degree in power electronics and electric drives from the College of Electrical Engineering, Zhejiang University, in 2000.

Since 2000, he has been a Faculty Member at Zhejiang University, teaching and conducting research on power electronics. He is currently an Associate Professor. His research interests include topologies and control for switch-mode power conversion. He is the corresponding author of this paper.

Xiangning He (M'95–SM'96–F'10) received the B.Sc. and M.Sc. degrees from the Nanjing University of Aeronautical and Astronautical, Nanjing, China, in 1982 and 1985, respectively, and the Ph.D. degree from Zhejiang University, Hangzhou, China, in 1989.

From 1985 to 1986, he was an Assistant Engineer at the 608 Institute of Aeronautical Industrial General Company, Zhuzhou, China. From 1989 to 1991, he was a Lecturer at Zhejiang University. In 1991, he received a Fellowship from the Royal Society of U.K., and conducted research in the Department of Computing and Electrical Engineering, Heriot-Watt University, Edinburgh, U.K., as a Postdoctoral Research Fellow for two years. In 1994, he joined Zhejiang University as an Associate Professor. Since 1996, he has been a Full Professor in the College of Electrical Engineering, Zhejiang University. He was the Director of the Power Electronics Research Institute and the Head of the Department of Applied Electronics, and he is currently the Vice Dean of the College of Electrical Engineering, Zhejiang University. His research interests include power electronics and their industrial applications. He is the author or coauthor of more than 280 papers and one book "Theory and Applications of Multi-level Converters," Beijing, China: China Machine Press, 2006. He holds 22 patents.

Dr. He received the 1989 Excellent Ph.D. Graduate Award, the 1995 Elite Prize Excellence Award, the 1996 Outstanding Young Staff Member Award, and 2006 Excellent Staff Award from Zhejiang University for his teaching and research contributions. He received seven Scientific and Technological Achievements Awards from Zhejiang Provincial Government and the State Educational Ministry of China in 1998, 2002, 2009, and 2011, respectively, and six Excellent Paper Awards. He has been appointed as an IEEE Distinguished Lecturer by the IEEE Power Electronics Society in 2011. He is also a Fellow of the Institution of Engineering and Technology (formerly IEE), U.K.